Materials Futures

PAPER • **OPEN ACCESS**

The interplay between (electro)chemical and (chemo)mechanical effects in the cycling performance of thiophosphate-based solid-state batteries

To cite this article: Jun Hao Teo *et al* 2022 *Mater. Futures* **1** 015102

OPEN ACCESS
IOP Publishing | Songshan Lake Materials Laboratory
Materials Futures
Mater. Futures 1 (2022) 015102 (13pp)
https://doi.org/10.1088/2752-5724/ac3897

The interplay between (electro)chemical and (chemo)mechanical effects in the cycling performance of thiophosphate-based solid-state batteries

Jun Hao Teo[1], Florian Strauss[1], Felix Walther[2], Yuan Ma[1], Seyedhosein Payandeh[1], Torsten Scherer[3], Matteo Bianchini[1,4], Jürgen Janek[1,2,*] and Torsten Brezesinski[1,*]

[1] Battery and Electrochemistry Laboratory, Institute of Nanotechnology, Karlsruhe Institute of Technology (KIT), Hermann-von-Helmholtz-Platz 1, 76344 Eggenstein-Leopoldshafen, Germany
[2] Institute of Physical Chemistry & Center for Materials Research, Justus-Liebig-University Giessen, Heinrich-Buff-Ring 17, 35392 Giessen, Germany
[3] KNMF Laboratory for Micro- and Nanostructuring, Institute of Nanotechnology, Karlsruhe Institute of Technology (KIT), Hermann-von-Helmholtz-Platz 1, 76344 Eggenstein-Leopoldshafen, Germany
[4] BASF SE, Carl-Bosch-Str. 38, 67056 Ludwigshafen, Germany

E-mail: juergen.janek@kit.edu and torsten.brezesinski@kit.edu

Received 7 October 2021, revised 10 November 2021
Accepted for publication 10 November 2021
Published 12 January 2022

Abstract

Solid-state batteries (SSBs) are a promising next step in electrochemical energy storage but are plagued by a number of problems. In this study, we demonstrate the recurring issue of mechanical degradation because of volume changes in layered Ni-rich oxide cathode materials in thiophosphate-based SSBs. Specifically, we explore superionic solid electrolytes (SEs) of different crystallinity, namely glassy $1.5Li_2S$-$0.5P_2S_5$-LiI and argyrodite Li_6PS_5Cl, with emphasis on how they affect the cyclability of slurry-cast cathodes with NCM622 (60% Ni) or NCM851005 (85% Ni). The application of a combination of *ex situ* and *in situ* analytical techniques helped to reveal the benefits of using a SE with a low Young's modulus. Through a synergistic interplay of (electro)chemical and (chemo)mechanical effects, the glassy SE employed in this work was able to achieve robust and stable interfaces, enabling intimate contact with the cathode material while at the same time mitigating volume changes. Our results emphasize the importance of considering chemical, electrochemical, and mechanical properties to realize long-term cycling performance in high-loading SSBs.

* Authors to whom any correspondence should be addressed.

Supplementary material for this article is available online

Keywords: solid-state battery, slurry casting, lithium thiophosphate electrolyte, Ni-rich NCM cathode, degradation

(Some figures may appear in colour only in the online journal)

Future perspectives
The increasing demand for energy-dense CAMs has been a driving force toward layered Ni-rich oxides. This inevitably leads to modifications in cathode composite design, requiring solutions that can mitigate the volumetric changes during electrochemical cycling. Looking from the materials perspective, a viable approach, as demonstrated herein, is the use of a 'soft' SE that is capable of producing robust and stable interfaces, especially with the CAM, and maintaining tight contact even upon severe volume changes. Nevertheless, future studies are required to ascertain the properties of the degradation products as well as their formation mechanism(s), since this study indicated the large influence the composition of the CAM/SE interface has on the overall cell cyclability. Another approach would be the design of low-strain or single-crystalline CAMs, the latter of which have been reported to show increased resistance to cracking both during preparation and cycling. On the other hand, optimizing the electrode formulation and cycling conditions may help accommodate for the volume expansion/contraction, thus enabling the use of Ni-rich NCM CAMs with a larger variety of SEs. Apart from that, newly established analytical techniques in LIB research, such as acoustic emission monitoring, could be employed to probe the void/crack formation in SSBs. Lastly, it should be noted that all of the above considerations have not yet taken into account the (chemo)mechanical and (electro)chemical effects at the negative electrode side. With silicon (Si), a material that is known for undergoing extremely large relative volume changes during cycling, becoming attractive for SSB applications, an already optimized cathode would be beneficial when developing solutions for the anode.

1. Introduction

With the advance in technology ranging from mobile devices to electric vehicles and a global push toward renewable resources (away from fossil fuels), research in electrochemical energy storage has been catapulted to a position front and center. The past three decades have seen rapid adoption in the use of liquid electrolyte-based lithium-ion batteries (LIBs) [1–3]. However, LIBs have limitations, such as the inherent safety problems caused by flammable components in the system and the limited temperature window for operation [2, 4, 5]. Moreover, they are approaching their theoretical energy densities. These limitations could be theoretically overcome with the inception of solid-state batteries (SSBs), i.e. replacing the liquid electrolyte by a solid electrolyte (SE). With their promise of increased gravimetric and volumetric energy densities by allowing the use of lithium-metal anodes as well as offering improved safety conditions and larger operating temperature windows, SSBs could be applied in a wider range of applications [6]. However, they possess their own inherent problems. One persisting problem is the rapid capacity fade usually observed for SSBs, which can be attributed to an interplay between (electro)chemical and (chemo)mechanical processes [7–9]. The net effect of either process on the capacity retention depends primarily on the choice of materials and their mutual interactions.

In this study, we focus on industrially relevant materials, with the cathode active material (CAM) being a layered Ni-rich oxide, $Li_{1+x}(Ni_{0.6}Co_{0.2}Mn_{0.2})_{1-x}O_2$ (NCM622) or $Li_{1+x}(Ni_{0.85}Co_{0.10}Mn_{0.05})_{1-x}O_2$ (NCM851005), and the SEs being lithium thiophosphates. Layered oxide CAMs are well established in LIBs and are also very attractive for use in SSBs. However, they undergo distinct volume changes upon (de)lithiation, making the selection of the other components of the composite even more important [10–12]. Regarding the SE, sulfides (thiophosphates) are a popular choice for SSBs. Their low Young's moduli enable an increased mechanical integrity of the cell [13–16]. In addition, they are easy to be processed and show highly competitive ionic conductivities, with some reaching values as high as 10^{-2} S cm^{-1} at room temperature [17]. Nevertheless, sulfide SEs exhibit poor (electro)chemical stability, often featuring significant interfacial decomposition at both low and high voltages [18]. This (electro)chemical instability has been studied to a great extent and addressed in various publications [19–21]. A widely adopted solution to overcome stability issues, for example, is the application of surface coating strategies to the electrode materials [22–27]. The mechanical degradation, on the other hand, and its underlying mechanism(s) and contribution to capacity fading have not been fully understood and are subject of recent works [28–32]. One approach to alleviate the capacity fading caused by such effects is to tailor the material's mechanical properties, such as the use of a glassy SE phase instead of a crystalline one. Another possibility is to optimize the cycling conditions (e.g. cutoff voltage, anode/cathode ratio, etc) to mitigate volume changes of the active material, especially during the initial cycles [33, 34]. Herein, we chose to focus on the former, which has shown promise in the past. For example, Wang *et al* recently investigated the impact of crystallinity on the (chemo)mechanics and showed that the higher ionic conductivity that comes with it does not necessarily guarantee improved capacity retention [28]. Moreover, Minnmann *et al* demonstrated that the effective ionic conductivity of crystalline sulfide SEs in NCM-based cathode composites decreases up to an order of magnitude compared to

the bulk SE [35]. Similarly, we have recently reported electrochemical data for pelletized SSBs with two different thiophosphate SEs, namely glassy $1.5Li_2S$-$0.5P_2S_5$-LiI (referred to as g-SE) and argyrodite Li_6PS_5Cl (referred to as c-SE), with the former showing superior cycling stability [29].

The capacity retention after 200 cycles was found to be ∼58 and 39% for the g-SE and c-SE cells, respectively (figure S1 (available online at stacks.iop.org/MF/1/015102/mmedia)). Interestingly, the capacity delivered by the c-SE cell continued to decline strongly even after 200 cycles. We also noticed a difference in the Coulombic efficiency. While it increased steadily for the g-SE cell, reaching a value above 99.5% after 50 cycles, the c-SE cell exhibited a different trend. It was able to achieve 99.4% within 20 cycles, then the Coulombic efficiency decreased in the subsequent cycling until a local minimum around 40 cycles was reached, followed by a new increase beyond 99.5% only after 150 cycles. It should be noted that the crystalline Li_4PS_4I counterpart was not used for comparison because of its relatively poor room-temperature ionic conductivity. Instead, argyrodite Li_6PS_5Cl was chosen as SE. In this work, we aim to build upon our results by utilizing different *ex situ* and *in situ* analytical techniques to better understand the interplay between (electro)chemical and (chemo)mechanical effects and their influence on the long-term cyclability of SSB cells using a slurry-cast cathode.

2. Results

2.1. Cell performance

With our previous data in mind, we attempted a similar electrochemical analysis for slurry-cast cathodes (figure 1). The components included $LiNbO_3$-coated NCM622 CAM, glassy $1.5Li_2S$-$0.5P_2S_5$-LiI or argyrodite Li_6PS_5Cl as SE, Super C65 carbon black additive, and a polyisobutene (Oppanol) binder. The SSB cells were cycled with a similar protocol as the pelletized (powder-based) cells in the voltage range of 1.35–2.85 V vs $Li_4Ti_5O_{12}/Li_7Ti_5O_{12}$ (approximately 2.9–4.4 V vs Li^+/Li) at a C/5 rate and 45 °C for 200 cycles (see section 4 for more details). Interestingly, the g-SE cell exhibited excellent cycling performance and stability (figure 1(a)). The first-cycle specific charge and discharge capacities were 190 and 162 mAh/g_{NCM622}, respectively. Despite the slightly lower values at the beginning of the cycling experiment compared to the corresponding pelletized cell, the slurry-cast cell showed a much improved capacity retention of ∼87 vs 58% after 200 cycles, corresponding to a fade rate per cycle of only 0.065% (∼3.3 times lower than for the pelletized cell). Especially the Coulombic efficiency data indicated a strong stabilization from the 4th cycle onward (>99%). However, this kind of improved electrochemical performance was not observed for the slurry-cast c-SE cell (figure 1(b)). The first-cycle specific charge and discharge capacities were 200 and 171 mAh/g_{NCM622}, respectively. The capacity retention after 200 cycles was ∼49%, which is only moderately higher compared to the pelletized cell with ∼39%. In this case, the margin of 10% improvement in capacity

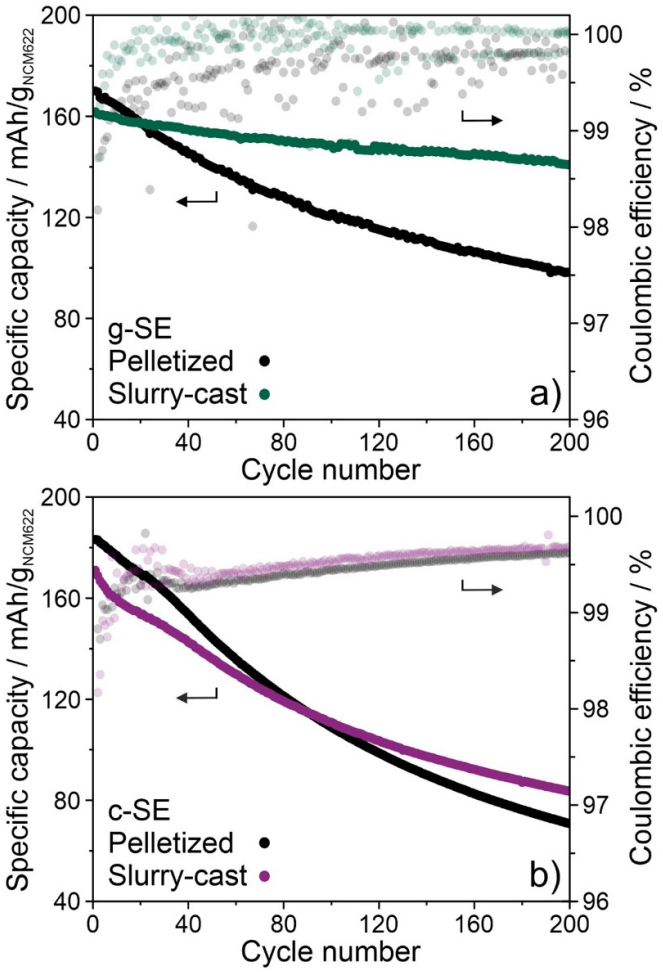

Figure 1. Cycling performance of SSB cells with (a) glassy SE ($1.5Li_2S$-$0.5P_2S_5$-LiI) and (b) crystalline SE (Li_6PS_5Cl) in both pelletized and slurry-cast cathodes and corresponding Coulombic efficiencies. Cells tested at 45 °C, C/5, 2.9–4.4 V vs Li^+/Li.

retention is too small to conclude that a slurry-cast cathode performs better than a pelletized one when using the argyrodite SE.

2.2. Cross-sectional scanning electron microscopy (SEM) imaging

Transitioning to the slurry-cast cathodes, we noticed a much larger improvement for the g-SE cell over the crystalline one. The g-SE cell exhibited a ∼29% increase in capacity retention (over 200 cycles), compared to a ∼10% improvement in the c-SE cell. It has been reported that slurry-based casting processes improve the homogeneity of distribution within the cathode composite and the interfacial contact between CAM and SE [36, 37]. A morphological comparison between the pelletized and slurry-cast cathodes for the argyrodite SE via SEM showed that the use of a wet-chemical process (solvent-based mixing) reduces voids and increases the particle-particle contact (figure S2). However, even with better interfacial contact at the beginning of cyc-

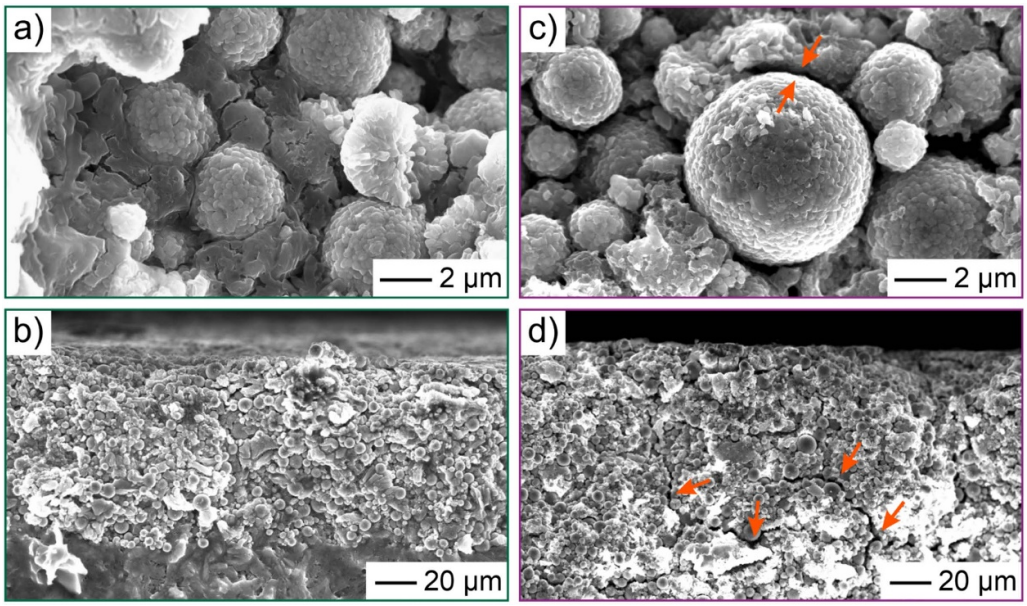

Figure 2. Cross-sectional SEM images of the slurry-cast cathode of SSB cells using (a), (b) glassy SE ($1.5Li_2S$-$0.5P_2S_5$-LiI) and (c), (d) crystalline SE (Li_6PS_5Cl) after 200 cycles at a rate of C/5 and 45 °C. The arrows denote void formation and cracking.

ling, the capacity fading was still prominent in the c-SE cell. To that end, cross-sectional SEM was performed on the slurry-cast cathodes after 200 cycles (figures 2(a)–(d)). From the images, it is apparent that the c-SE electrode exhibited a larger fraction of void space around the CAM secondary particles and intergranular cracks compared to the g-SE electrode. The voids (prevalent in the c-SE cell) have been reported in literature to result from the mechanical separation between CAM and SE [18, 30, 38]. (Chemo)mechanically-driven separations and possible cracking, typically due to volume changes during cycling, with $\Delta V/V \approx -3\%$ at 4.4 V vs Li^+/Li for NCM622 in LIBs [10, 32], would lead to less electrochemically active contact area (material), thereby adversely affecting the reversibility and capacity retention. The images suggest that even with improved interfacial contact, mechanical separation occurs if the SE does not possess the necessary mechanical properties required for mitigation of void formation/cracking. On a side note, the protective coating ($LiNbO_3$) plays a minor or no direct role in contributing to mitigating (chemo)mechanically-driven separations. In a recent publication, Ma *et al* showed that there are no major differences in CAM/SE contact between (cycled) cathodes using uncoated and $LiNbO_3$-coated $LiNiO_2$ [9]. However, indirectly, the coating plays a role in the formation of interfacial degradation products, which possess their own inherent (electro)chemical and (chemo)mechanical properties. While the (electro)chemical aspect can be examined by observing the cycling behavior, the (chemo)mechanical aspect remains elusive. Nevertheless, the objective of this study was the comparison of (electro)chemical and (chemo)mechanical properties from the SE point of view, thus the role of the coating will not be elaborated upon any further.

In the following sections, a more in-depth analysis into the ability of the glassy SE to alleviate (chemo)mechanical effects in slurry-cast cathodes will be conducted. This encompasses study of the interfacial degradation via electrochemical impedance spectroscopy (EIS), differential electrochemical mass spectrometry (DEMS), x-ray photoelectron spectroscopy (XPS), and time-of-flight secondary ion mass spectrometry (ToF-SIMS).

2.3. EIS

EIS was performed to better understand the correlation between void/crack formation and electrochemical performance. The Nyquist plots of the electrochemical impedance after cycling and corresponding fits to the data are shown in figure 3. Fitting was done assuming an $R_1(R_2/Q_2)(R_3/Q_3)(R_4/Q_4)$ equivalent circuit. R_1 is the resistance of the bulk (separator) SE, R_2 the SE grain boundary (gb) resistance, R_3 the cathode (CAM/SE) interfacial resistance, and R_4 represents the anode (anode active material (AAM)/SE) interfacial resistance [18, 39, 40]. The SE bulk (area specific) resistance was ∼38.2 and 15.9 Ω cm^2 for the g-SE and c-SE cells, respectively. This difference can be explained by a more than doubled room-temperature ionic conductivity for the crystalline SE compared to the glassy SE (∼2.0 vs 0.8 mS cm^{-1}). Moreover, we found that the cathode interfacial resistance exhibited a larger value for the g-SE cell (∼8.3 Ω cm^2) than for the c-SE cell (∼2.5 Ω cm^2). The major factors contributing to the latter resistance are electrochemical decomposition of the SE (interfacial reaction between CAM and SE) and void/crack formation [28]. We assume that in case of the g-SE cell, the largest contribution to the $R_{CAM/SE}$ is the formation of a relatively thick layer of degradation products at this interface. The contribution of void formation and/or cracking is probably small, since no visible (chemo)mechanically-driven separation between CAM and SE was apparent from SEM imaging (figures 2(a) and (b)). On the other hand, the major contribution to the $R_{CAM/SE}$ for the c-SE cell can most

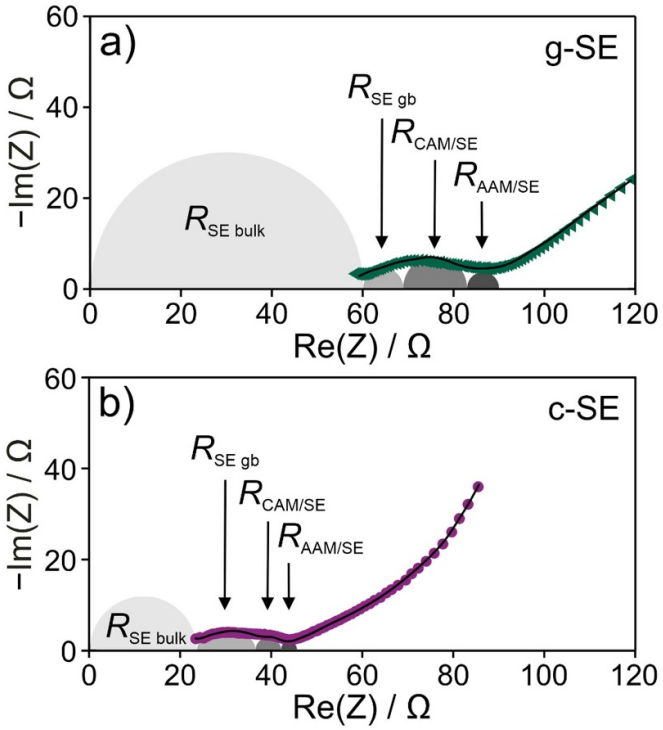

Figure 3. Nyquist plots of the electrochemical impedance of SSB cells (black lines: measured data; solid symbols: fitted data) using a slurry-cast cathode with (a) glassy SE ($1.5Li_2S$-$0.5P_2S_5$-LiI) and (b) crystalline SE (Li_6PS_5Cl) after 200 cycles at a rate of C/5 and 45 °C. Semicircles provide eye guidance for the individual resistance contributions.

likely be attributed to (chemo)mechanically-driven separation effects, as evidenced by the void/crack formation (figures 2(c) and (d)). To support this argument, we will incorporate solid-state diffusion into the analysis. The total cell impedance consists of the SE bulk resistance, the charge-transfer resistance, and the low-frequency Warburg component (equation S1). The Warburg coefficient having an inverse relationship with the contact area between CAM and SE can be represented as shown in equation S2 (see also figure S3 and accompanying explanation). While electrochemical degradation only affects the charge-transfer resistance, mechanical separation increases both the charge-transfer and Warburg resistances; both contributions can be distinguished. Overall, a larger Warburg coefficient (assuming that the lithium-diffusion coefficient is constant) means a smaller contact area and therefore a higher degree of mechanical separation. In fact, the Warburg coefficient for the c-SE cell was larger by a factor of about two compared to the g-SE cell, suggesting a lower contact area between CAM and SE after 200 cycles. Lastly, we observed a lower SE grain boundary resistance in the g-SE cell (~5.7 vs 8.3 Ω cm^2), which could be explained by the reduced degree of crystallinity. SE particle fracturing resulting from (chemo)mechanically-induced stress during cycling may also contribute to this difference, as indicated by the larger void fraction observed within the argyrodite SE in 3D reconstructions of focused ion beam (FIB)-SEM slice images of the electrodes (figure S4) [29].

Despite the lower cathode interfacial resistance of the c-SE cell, its electrochemical performance was drastically worse than the g-SE cell, indicating that mechanical separation more strongly affects the long-term cycling performance than electrochemical decomposition reactions do. In addition, the data suggest that the formation of 'self-limiting interphases' for the g-SE cell (>99% Coulombic efficiency after three cycles) might not be as detrimental to the cyclability as originally thought.

2.4. In situ *pressure monitoring*

Next, we attempted to elucidate the differences in void/crack formation via *in situ* pressure monitoring of the respective SSB cells [28, 30, 38]. The as-measured force response is shown in figure S5. The force response was corrected for its baseline and converted to pressure change (uniaxial stress, σ_{11}). To focus on the changes in stress in the slurry-cast composite cathodes, $Li_4Ti_5O_{12}$ (LTO) was used as AAM. LTO is a zero-strain electrode material, i.e. its relative volume changes upon cycling are negligible [41–43]. Among the various contributors to the changes in stress within the cathode, the expansion/contraction of the CAM dominated the pressure signal. During delithiation (charge cycle), a negative net pressure change (Δp) was recorded because of the volume contraction of the NCM622 [10]. Upon lithiation (discharge cycle), the volume change was reversed, leading to a positive net pressure change, at first sight independent of the SE. Following several cycles, a sudden decrease in Coulombic efficiency was seen, which was unique to the c-SE cell (figure S6). This confirms the non-monotonous nature of the Coulombic efficiency versus cycle number curve shown in figure 1(b) and could be an indication of (chemo)mechanically-driven separations between cathode constituents reaching a critical point [31, 44]. However, in the pressure measurements, probing primarily the CAM breathing, no distinct changes in stress response were observed. In fact, the pressure response was similar for both SEs, despite the g-SE cell using one with a lower Young's modulus (<14 GPa) [15, 45] compared to the c-SE cell (>22 GPa) [13]. This was to be expected because of the large fraction of CAM in the composite (>68 wt.%). The equipment used and the measuring conditions did not allow for resolving the subtle changes (to the pressure response) originating from (chemo)mechanical interactions involving the SE.

Therefore, model experiments attempting to remove the CAM contribution by using SE/carbon black electrodes were conducted. Specifically, cyclic voltammetric (CV) measurements were carried out for the different SE-based cells, and the corresponding pressure response during the first two cycles was recorded (figures 4(a)–(c) and (e)–(g)). A net pressure change was observed in both cases. The data showed a relatively large negative pressure response for the crystalline SE/Super C65 as opposed to a minor positive pressure response for the glassy SE/Super C65. Taking the current response into account, these pressure changes seem to be due to a more prominent electrochemical oxidation of the crystalline SE [46]. The increased electrochemical stability window of Li_2S-P_2S_5 SEs with LiI incorporation has also

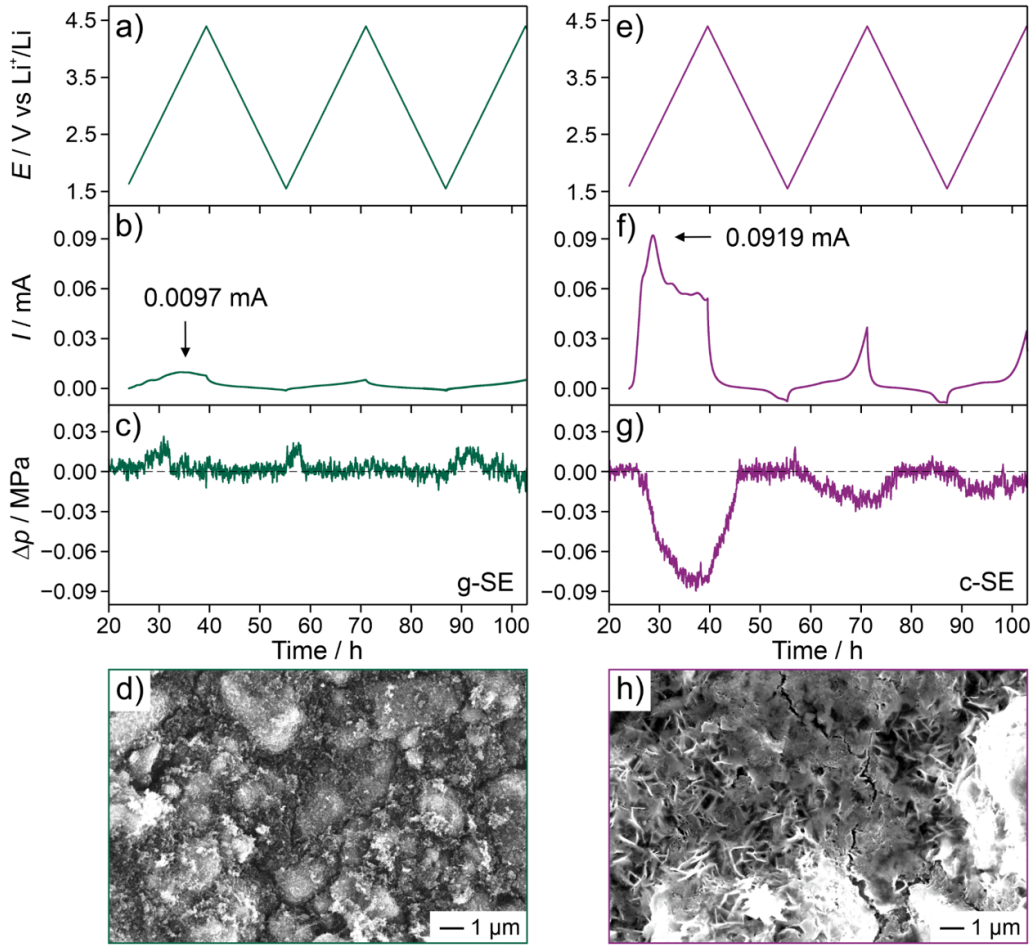

Figure 4. *In situ* pressure monitoring of Super C65 electrodes with (a)–(c) glassy SE ($1.5Li_2S$-$0.5P_2S_5$-LiI) and (e)–(g) crystalline SE (Li_6PS_5Cl). (a), (e) CV profiles, (b), (f) current response, and (c), (g) pressure response. Cells tested at 45 °C, 0.05 mV s^{-1}, OCV-4.4 V vs Li^+/Li in the first cycle and 1.55–4.4 V vs Li^+/Li in the following cycles. Top-view SEM images of the (d) glassy SE/Super C65 and (h) crystalline SE/Super C65 electrodes after cycling.

been reported in literature [47, 48]. This is further supported by the crack/void formation observed by SEM primarily for the crystalline SE/Super C65 electrode (figures 4(d) and (h)), a result of the shrinkage (volume contraction) of the SE. Additionally, in case of the crystalline SE/Super C65 electrode, the initial decrease in pressure was recovered during the cathodic sweep (reduction), indicating partial reversibility of the degradation processes [49]. On the other hand, the glassy SE/Super C65 electrode did not show a change in pressure in the cathodic sweep, suggesting that the degradation products formed are either redox inactive or do not lead to significant pressure changes. These findings help explain the observation of a quicker stabilization of the Coulombic efficiency above 99.5% (formation of robust/stable interfaces and ('self-limiting') interphases) and the good interfacial contact (no voids/cracks) for the glassy SE. Because the major part of side product formation occurs in the initial cycle, we noticed an opposing trend to the EIS measurements. However, it has to be noted that EIS was performed after 200 cycles and does not take into account the fast stabilization of the g-SE cell. Besides, the CAM is not present in this simple model experiment, and the (electro)chemical reaction between NCM622 and SE must also be considered in case of the EIS measurements.

2.5. In situ *gas analysis*

Building upon the observations from *in situ* pressure monitoring and reports on the impact of side product formation on the pressure evolution, a series of *ex situ* and *in situ* analytical techniques (DEMS, XPS, and ToF-SIMS) were used to characterize the chemical nature of the gaseous and solid degradation products for both SEs [28].

First, *in situ* gassing studies via DEMS were performed on the slurry-cast cathodes (figure 5). To this end, the SSB cells were cycled at a C/20 rate and 45 °C in the voltage range of 2.9–5.0 V vs Li^+/Li. The higher charge cutoff voltage was chosen with the intention of increasing the evolution of reactive oxygen from the NCM622 CAM and observing its reaction with the surrounding SE. The cells underwent three cycles and the gas evolution was monitored for $m/z = 1$–100. While four gases were detected for the g-SE cell (H_2, O_2, CO_2, and SO_2; see figure 5(a)), only three were detected for the c-SE cell (H_2, O_2, and CO_2; see figure 5(b)).

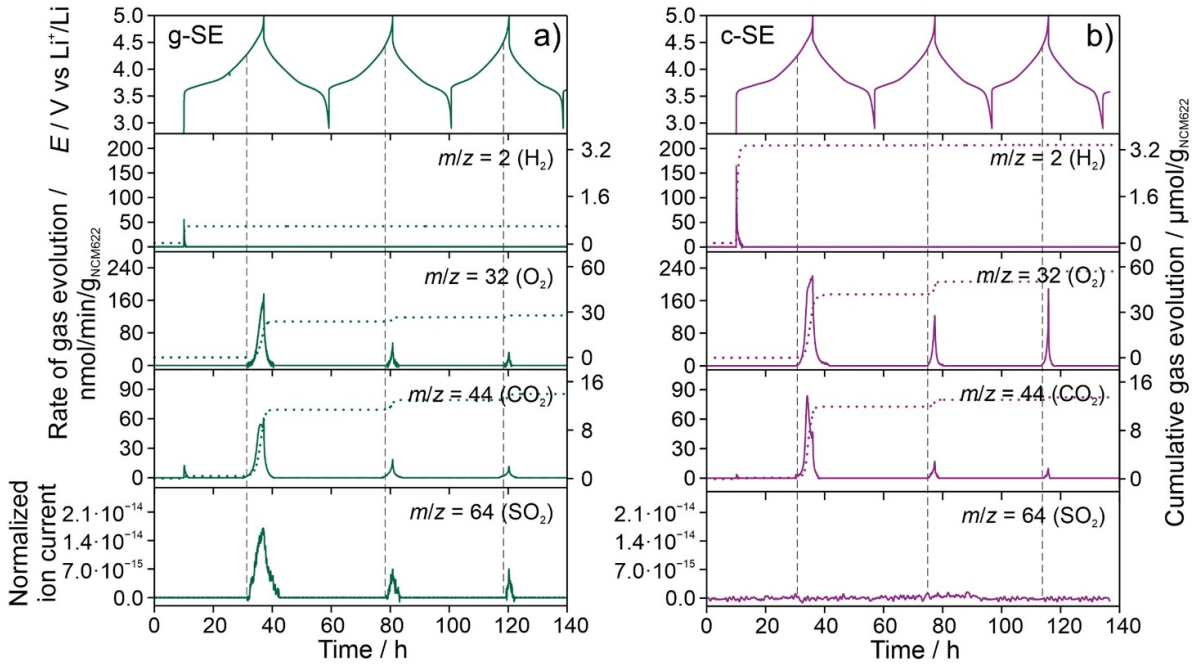

Figure 5. Electrochemical profile of SSB cells using a slurry-cast cathode with (a) glassy SE ($1.5Li_2S$-$0.5P_2S_5$-LiI) and (b) crystalline SE (Li_6PS_5Cl) and corresponding time-resolved evolution rates (left *y*-axis) and cumulative amounts (right *y*-axis) for H_2, O_2, and CO_2, as well as normalized ion currents for SO_2. Cells tested at 45 °C, C/20, 2.9–5.0 V vs Li^+/Li.

H_2 evolution ($m/z = 2$) occurred at the onset of the initial charge cycle and can most likely be related to the reduction of trace H_2O at the anode. For example, it has been reported that a charged LTO ($Li_7Ti_5O_{12}$) anode in LIBs undergoes redox reactions with H_2O, thereby producing H_2 [50]. The lithiated indium anode should follow a similar reaction pathway creating 0.5 mol of H_2 for every mol of H_2O. Interestingly, the cumulative amount of H_2 evolution was lower by a factor of around four for the g-SE cell compared to the c-SE cell (∼0.6 vs 3.4 μmol/g_{NCM622}). Given that both cathode composites were fabricated and processed identically with the only difference being the type of SE used, this result suggests that the reduction of residual H_2O is mitigated in the g-SE cell. Recently, it has been reported that Li_4PS_4I exhibits a high stability toward H_2O, partially routed in the formation of an LiI·H_2O adduct. The formation of such a phase might take place as well here, competing with the electrochemical reduction of H_2O and therefore H_2 release [51]. Nevertheless, in case of the c-SE cell, solely electrochemical reduction of H_2O traces occurs, being responsible for the increased amount of evolved H_2.

Regarding O_2 evolution, cells containing an NCM622 CAM are typically required to achieve a state of charge (SOC) ⩾80%. This condition was met with ∼89% (244 mAh/g_{NCM622}) and ∼85% (234 mAh/g_{NCM622}) for the g-SE and c-SE cells, respectively. Mass signals characteristic of O_2 ($m/z = 32$) with onset voltages of ∼4.3 V vs Li^+/Li were observed, in agreement with reports available in literature [37, 52–55]. The origin of O_2 (presumably at least partly in the form of $^1O_2$) evolution in layered Ni-rich oxide CAMs has been extensively studied in the past and shown to be a consequence of the destabilization of the crystal lattice at high SOC (due to either layered-to-spinel or layered-to-rocksalt transformation) [52, 53]. Prior to the physical decay of the highly reactive $^1O_2$ toward its triplet ground state [56], there is a possibility of the singlet oxygen reacting with the different components present in the cathode composite. Moreover, the amount of O_2 evolving should scale exponentially with the SOC [37]. Despite showing a lower SOC, the cumulative amount of molecular O_2 in the first cycle was ∼42 μmol/g_{NCM622} for the c-SE cell versus ∼23 μmol/g_{NCM622} for the g-SE cell. This difference seems explainable by the consumption of reactive oxygen through follow-up reactions with the thiophosphate SE, which appears to be facilitated for the g-SE cell because of the more intimate CAM/SE contact. In contrast, the c-SE cell showed increased particle distances from mechanical separations, apparently reducing the extent of oxidation reactions. Apart from that, the formation of voids is believed to affect the gas release from the bulk of the cathode to the surface.

We also monitored the evolution of SO_2, which is a common phenomenon for SSB cells containing sulfide SEs and is of utmost interest in this study. SO_2 formation and release is a clear indication of chemical oxidation of the thiophosphate SE. In case of the g-SE cell, a sharp peak corresponding to the mass signal $m/z = 64$ (normalized with respect to the carrier-gas signal $m/z = 4$ (He)) was detected at high SOC. SO_2 evolution has been reported to be a result of the chemical reaction between SE and reactive oxygen that is released from the CAM or the electrochemical decomposition of residual surface carbonates [55, 57, 58]. However, the exact reaction mechanism (degradation route) is unclear at present. While SO_2 was clearly detected in the g-SE cell, no SO_2 evolution was observed for the c-SE cell. This result strengthens the argument above, where

in case of the g-SE cell, the amount of released O_2 is decreased in favor of SO_2 formation because of the better CAM/SE contact. However, there remains the possibility that the increased SO_2 evolution is instead due to differences in composition and chemical stability/reactivity. The lower cumulative amount of O_2 for the g-SE cell could be attributed to the formation of non-gaseous, oxidized sulfur species, resulting in the consumption of reactive oxygen through side reactions (see section on XPS/ToF-SIMS characterization below).

Lastly, we monitored the CO_2 mass signal ($m/z = 44$). CO_2 evolution in SSB cells is typically indicated by sharp peaks with onset voltages $\geqslant$4.2 V. However, CO_2 release has also been observed at the beginning of the first charge cycle and postulated to be due to side reactions at the anode [37, 54, 55]. At high voltages, CO_2 evolution could stem from three possible sources: (a) electrochemical decomposition of residual surface carbonates present on the CAM particles, (b) chemical oxidation of the polymer binder, and (c) chemical oxidation of the carbon additive [37, 57]. The electrochemical decomposition of surface carbonates is reported to proceed by the process shown in equation S3 [58, 59]. While the mechanisms for sources (b) and (c) are largely unknown, they are indirectly observed by the coincidence of $m/z = 44$ and 32 signals at the highest SOC [37]. This suggests that beyond 4.8 V vs Li^+/Li, reactions between the carbon-related components (binder and additive) and the reactive oxygen are possible. Unsurprisingly, the cumulative CO_2 evolution was similar with $\sim$13.9 and 13.4 μmol/g_{NCM622} for the g-SE and c-SE cells, respectively. This is because CO_2 evolution is largely independent of the type of SE used and rather dependent on the CAM surface chemistry (carbonate impurities).

2.6. Interfacial degradation

Taken together, the gas analysis via DEMS revealed an increased formation of SO_2 in the g-SE cell because of chemical oxidation of the SE with reactive oxygen species released by the CAM. To further investigate the interfacial reactions occurring in the slurry-cast cathodes, we utilized a combination of post-mortem XPS and ToF-SIMS and studied the formation of solid side products after 200 cycles.

Typical of thiophosphate-based SSBs, analysis of the S 2p and P 2p core-level spectra before and after cycling was conducted to probe the degradation products at the CAM/SE interface. The XPS data in figure 6 were taken after 480 s sputtering to mitigate any detrimental effects from the current collector [27, 60]. The S 2p signals for the uncycled g-SE and c-SE cells were fitted with three doublets (figure 6(a)). The first doublet with binding energies of 160.1/161.4 eV (gray component) represents the 'free' S^{2-} ions from the SE crystal structure and/or Li_2S impurities [27, 46, 49, 60–63]. The relative signal intensity of this doublet decreased upon cycling because of oxidation reactions occurring during charge, with the decrease being more prominent in the g-SE cell. While the doublet was still present after 200 cycles for the c-SE cell, it was not detectable anymore for the g-SE cell. The second doublet at 161.7/162.7 eV corresponds to the PS_4^{3-} tetrahedra (red component). The third doublet at 162.9/164.1 eV (blue component) can be attributed to various compounds. On the one hand, this includes anionic frameworks that thiophosphate SE phases can pass through toward the formation of P_2S_5 [46, 62]. On the other hand, the doublet may arise from oxidized sulfur species (polysulfides) [61, 63]. Note that the signal position of polysulfides depends on the chain length and gradually approaches the theoretical binding energy of elemental sulfur [27]. The pronounced signal intensity and broadening of this doublet for the g-SE cell may either indicate stronger degradation reactions or the presence of thiophosphate anions, i.e. $P_2S_7^{4-}$ and $P_2S_6^{2-}$, in agreement with Raman spectroscopy data obtained on related $x$$Li_2S$-$y$$P_2S_5$-$z$LiI phases [16, 48, 62–64]. After cycling, the g-SE cell showed a more severe degradation of the sulfur species, apparent by an increase in signal contributions at higher binding energies. The electrochemical decomposition reactions of the SE can, in principle, occur at all interfaces allowing electron transfer in the cathode, i.e. toward the current collector, the carbon additive, and the CAM, assuming the polymer binder to be electronically insulating [27]. Hence, this observation cannot be directly attributed to a specific interface and/or differences in the thermodynamic stability window of the SE. However, the S 2p spectrum for the g-SE cell showed an additional weak component around 170 eV, not observed for the c-SE cell. This signal is typically related to oxygenated sulfur species in thiophosphate-based SSBs [49]. Because the NCM622 is the only oxygen source in the cathode, it can be directly attributed to CAM/SE interfacial degradation reactions. This result thus indicates either an increased oxygen-involving degradation because of the tight contact between CAM and SE for the g-SE cell or a poorer chemical stability of the glassy SE against reactive oxygen. Nevertheless, the stronger signal of oxygenated sulfur species agrees with the more significant SO_2 evolution discussed above.

For the interpretation of P 2p data, the spectrum is usually deconvoluted into three contributions (figure 6(b)). The main contribution was fitted with a doublet having binding energies of 131.9/133 eV (red component) and can be assigned to the PS_4^{3-} tetrahedra [49, 61, 63]. The c-SE cell did not show additional signal contributions prior to cycling. However, a shoulder evolved at higher binding energies upon cycling, which we relate to the overlapping of newly formed doublets, analogous to the S 2p spectra (doublet at 133.2/133.9 eV (blue component), anionic framework transitions and phosphorus-containing polysulfide species; doublet at 134.4/135.4 eV (orange component), oxygenated phosphorus species, such as Li_3PO_4 and/or transition-metal phosphates). Especially the latter degradation products are believed to cause impedance buildup at the cathode side [63, 65]. Again, because the only oxygen source is the NCM622, the appearance of the doublet at 134.4/135.4 eV is indicative of adverse oxygen-involving side reactions at the CAM/SE interface. As somewhat expected, the higher binding-energy signals were more distinct for the g-SE cell than for the c-SE cell.

Finally, ToF-SIMS analysis was used to gain further insights into the interfacial degradation reactions. The high sensitivity of ToF-SIMS allows to investigate side products below the detection limit of XPS. However, ToF-SIMS is a semi-quantitative method and direct comparison of secondary

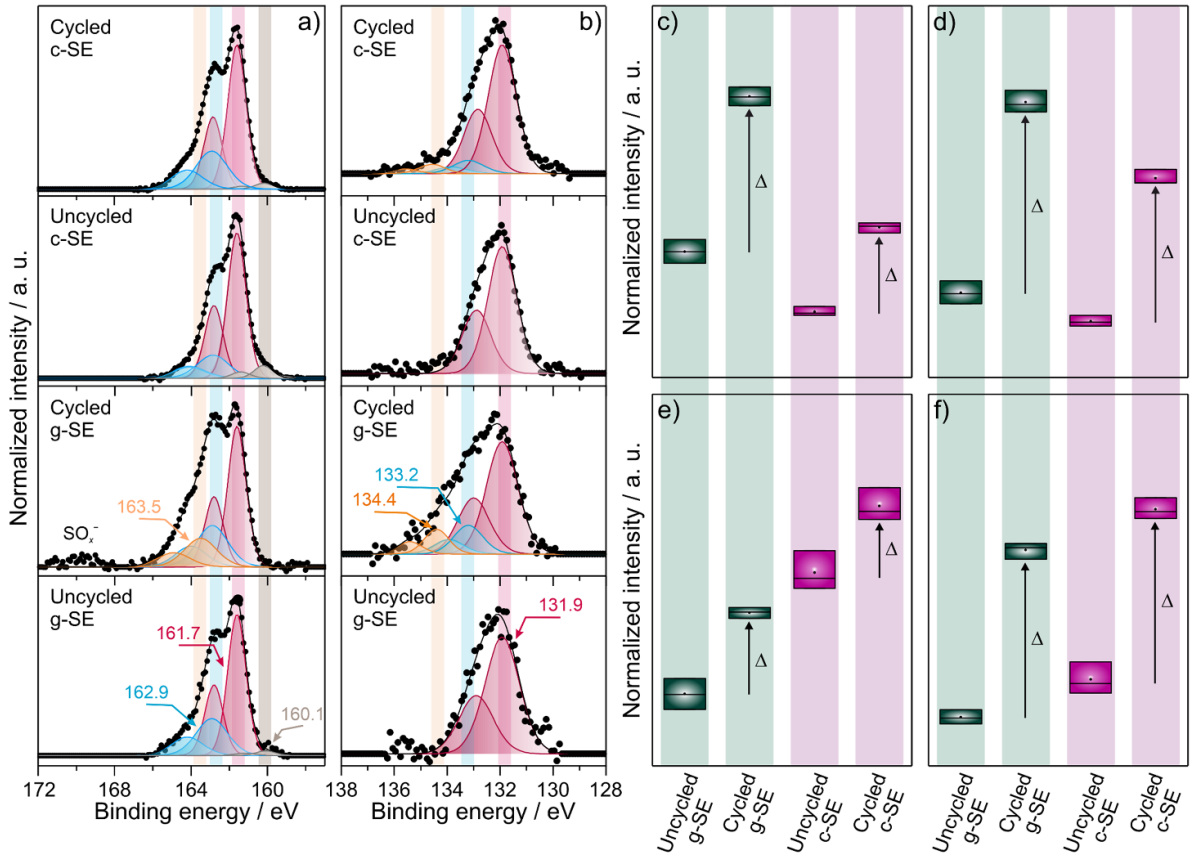

Figure 6. X-ray photoelectron spectra of the (a) S 2p and (b) P 2p core levels of slurry-cast cathodes with glassy SE ($1.5Li_2S$-$0.5P_2S_5$-LiI) and crystalline SE (Li_6PS_5Cl) collected before and after 200 cycles at a rate of C/5 and 45 °C. Box plots of the normalized intensity of (c) PO_2^-, (d) PO_3^-, (e) SO_2^-, and (f) SO_3^- fragments for the uncycled and cycled g-SE and c-SE cells from ToF-SIMS depth-profiling analysis.

ion intensities presupposes an identical chemical matrix. The matrix strongly determines the ionization probability and therefore the signal intensity of the charged fragments. Because SEs with a slightly different chemical composition were used in this study, a direct comparison of normalized intensities is not possible. For this reason, we considered the two systems independently, without comparing absolute values. Instead, the relative signal changes from uncycled to cycled cells were compared to assess differences in the degree of degradation. Figures 6(c)–(f) show results from ToF-SIMS depth-profiling experiments. The first ten scans of the profiles were excluded in the evaluation to minimize detrimental effects from the current collector. The PO_x^- and SO_x^- fragments ($2 \leqslant x \leqslant 3$) increased in both cases upon cycling. A comparison of the relative signal increase (Δ) between the g-SE and c-SE cells revealed an increased oxygen-involving degradation for the cathode using the glassy SE. This is in line with the XPS and DEMS results. However, keeping in mind the Coulombic efficiency of the g-SE cell, the majority of the interfacial degradation products should have formed within the first few cycles. Moreover, they appear to be stable over the course of cycling.

Overall, the experimental data agree well with each other and point toward the fact that there is a more intimate contact between CAM and SE for the g-SE cell. Although interfacial reactions (as seen in the initial cycles for the g-SE cell) are known to adversely affect the cell impedance, the contact loss (in the c-SE cell) apparently has a stronger effect on the battery performance. The favorable formation of stable ('self-limiting') interphases adds to the (chemo)mechanical stability in the g-SE cell by ensuring tight CAM/SE contact. Coupled with the already improved mechanical properties from the lower Young's modulus, this leads to a well-performing cell. In conclusion, the present work shows that (chemo)mechanical and (electro)chemical effects are mutually dependent and superimposed in the cycling data. If not considered carefully, this may lead to misleading interpretations.

2.7. Pushing the (chemo)mechanical limit

The beneficial properties of the glassy SE can also provide similar stability to NCM CAMs with an even higher Ni content (exemplified here for NCM851005), which naturally experience larger relative volume changes during cycling ($\Delta V/V \approx -6.5\%$ at 4.4 V vs Li^+/Li for NCM851005 in LIBs) [10, 32]. The slurry-cast NCM851005 cell was cycled under identical conditions (C/5, 45 °C) and in the same voltage range of 1.35–2.85 V vs $Li_4Ti_5O_{12}$/$Li_7Ti_5O_{12}$ (approximately 2.9–4.4 V vs Li^+/Li) as the slurry-cast NCM622 g-SE cell described above (figure 7). The first-cycle specific charge and discharge capacities were 210 and 177 mAh/$g_{NCM851005}$ (~2.7 mAh cm^{-2}), respectively, corresponding to an initial

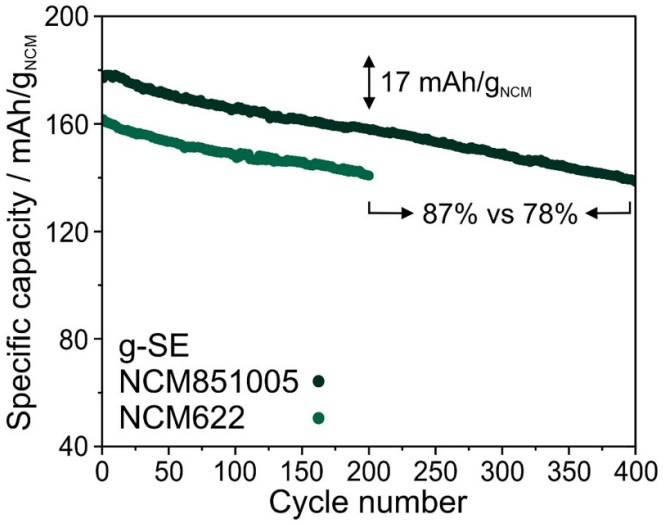

Figure 7. Cycling performance of SSB cells using a slurry-cast cathode with NCM622 (see also figure 1(a)) or NCM851005 and with glassy SE ($1.5Li_2S$-$0.5P_2S_5$-LiI). Cells tested at 45 °C, C/5, 2.9–4.4 V vs Li^+/Li.

Coulombic efficiency of 84%. The cell was able to show an extremely competitive capacity retention of ∼78% after 400 cycles (∼2.1 mAh cm^{-2}) with a fade rate per cycle of only 0.054%, compared to 0.065% for the NCM622 (over 200 cycles).

3. Conclusion

Herein, we have investigated the influence of a glassy ($1.5Li_2S$-$0.5P_2S_5$-LiI) and crystalline (Li_6PS_5Cl) thiophosphate SE on the cyclability of pelletized and slurry-cast SSB cells. We demonstrate that (chemo)mechanical and (electro)chemical effects contribute to the overall better performance for the glassy SE. These effects are interconnected and were elucidated with *ex situ* and *in situ* analytical techniques. The (chemo)mechanical effects were probed using pressure monitoring, for example, revealing an alternating increase/decrease in pressure during cycling (breathing of CAM), thus causing void/crack formation in case of the c-SE cell. In contrast, the g-SE cell exhibited signs of accommodating for such pressure changes, which seems highly beneficial to the cycling stability. Finally, gaseous and solid degradation products evolving at the CAM/SE interface were analyzed via DEMS, EIS, XPS, and ToF-SIMS. From these results, we conclude that the g-SE cell is more prone to interfacial degradation. However, given the excellent electrochemical performance, it is clear that the degradation products must be stable and sufficiently (ionically) conductive to allow for reversible battery operation [66].

Ultimately, considering all research data presented in this work, we state that for the studied compositions, the (chemo)mechanical benefits of a using a glassy SE outweigh the increased decomposition for the good of the SSB performance. The sacrifice in capacity over the first few cycles for improved capacity retention shows that the composition of the as-formed CAM/SE interface is of prime importance and strongly dictates the cyclability.

4. Methods

4.1. Materials and synthesis

Cells were prepared using $LiNbO_3$-coated $Li_{1+x}(Ni_{0.6}Co_{0.2}Mn_{0.2})_{1-x}O_2$ (NCM622, BASF SE) or $LiNbO_3$-coated $Li_{1+x}(Ni_{0.85}Co_{0.10}Mn_{0.05})_{1-x}O_2$ (NCM851005, BASF SE) powder as CAM [25]. Two SEs, glassy $1.5Li_2S$-$0.5P_2S_5$-LiI and argyrodite Li_6PS_5Cl (NEI Corp.), with room-temperature ionic conductivities of ∼0.8 and 2 mS cm^{-1}, respectively, were used. Glassy $1.5Li_2S$-$0.5P_2S_5$-LiI was synthesized by mixing stoichiometric amounts of Li_2S (99.9%, Sigma Aldrich), P_2S_5 (99%, Sigma Aldrich), and LiI (99.99%, Alfa Aesar) in a planetary ball-mill (Fritsch) under an Ar atmosphere for 12 h at 450 rpm using a 70 ml zirconia jar [29]. Li_6PS_5Cl was used as received. Polyisobutene (OPN, OPPANOL N 150, $M_w = 3.1{\cdot}10^6$ g mol^{-1}, BASF SE) was used as binder for the study. Super C65 carbon black (TIMCAL) as an electronically conductive additive was dried at 300 °C in a vacuum overnight prior to use. $LiNbO_3$-coated NCM was prepared by coating a 1 wt.% sol-gel $LiNbO_3$ layer onto the pristine CAM [25]. Carbon-coated $Li_4Ti_5O_{12}$ (LTO, NEI Corp.) was used as AAM. All materials were handled and stored in an Ar-filled glovebox from MBraun ($[O_2] < 0.1$ ppm, $[H_2O] < 0.5$ ppm).

4.2. Preparation of pelletized electrode composites

The cathode composite was prepared by planetary mixing $LiNbO_3$-coated NCM622 with either glassy $1.5Li_2S$-$0.5P_2S_5$-LiI or argyrodite Li_6PS_5Cl SE and Super C65 carbon black (7:3:0.1 weight ratio) under an Ar atmosphere for 30 min at 140 rpm [29]. The anode composite was prepared in a similar fashion by planetary mixing carbon-coated LTO with either glassy $1.5Li_2S$-$0.5P_2S_5$-LiI or argyrodite Li_6PS_5Cl SE and Super C65 carbon black (3:6:1 weight ratio).

4.3. Preparation of cathode sheets

The cathode composite contained $LiNbO_3$-coated NCM622 (or $LiNbO_3$-coated NCM851005), Super C65, OPN, and either glassy $1.5Li_2S$-$0.5P_2S_5$-LiI or argyrodite Li_6PS_5Cl SE. Their quantities were calculated to achieve an electrode with 1 wt.% polymer binder. Preparation of the cathode composite sheet involved a series of mixing steps, which are described in detail elsewhere [37]. The slurry was coated onto an Al foil with a mini-tape casting coater from MTI Corp. (300 μm doctor-blade slit size). Finally, the electrode was dried at room temperature in a two-step drying process. All chemicals and processing steps were handled in an Ar environment (Jacomex glovebox with $[O_2] < 1.0$ ppm and $[H_2O] < 1.0$ ppm).

4.4. Cell assembly and electrochemical testing

A customized setup was used for both the powder and slurry-cast cells. For the pelletized cell, 100 mg of SE was compressed at 125 MPa. Following, ∼11 mg (∼1.8 mAh cm^{-2}) of cathode composite was placed on top of the separator layer and subsequently compressed at 375 MPa. Lastly, 60 mg of anode composite was pressed onto the other side of the separator layer at 125 MPa (∼200 μm thickness). For the slurry-cast cell, both the sequence of assembly steps and the applied pressures were identical. The only difference was the cathode. Cathode sheet was punched out into a circular geometry (9 mm diameter; g-SE cell: ∼3.5 mAh cm^{-2}, c-SE cell: ∼3.2 mAh cm^{-2}) and placed on top of the separator layer. During electrochemical testing, a stack pressure of 80 MPa was maintained. Galvanostatic cycling was done at a rate of C/5 (1 C = 180 mA/g_{NCM622} or 190 mA/$g_{NCM851005}$) and 45 °C in the voltage range of 1.35–2.85 V vs $Li_4Ti_5O_{12}$/$Li_7Ti_5O_{12}$ using a MACCOR battery cycler. All cells were kept at 1 h open-circuit voltage (OCV) prior to cycling.

4.5. EIS

EIS measurements were conducted on cells after 200 cycles (C/5, 45 °C) using a SP-300 potentiostat (BioLogic). Spectra were collected in the frequency range between 100 mHz and 7.0 MHz with an AC voltage amplitude of 10 mV and fitted using the EC-lab software (BioLogic).

4.6. In situ *pressure monitoring*

After assembling the cell in the same customized setup used for electrochemical testing, it was packed in a pouch bag and removed from the glovebox. The rigid frame that was used to maintain the stack pressure was modified to accommodate an additional force sensor (KM26 10 kN, ME-Meßsysteme GmbH). The sealed cell with the force sensor was sandwiched within the custom frame and an initial pressure of 80 MPa was set. The stack was then placed in a heating chamber at 45 °C. Prior to the beginning of a similar galvanostatic charge/discharge measurement, a 24 h OCV period was maintained. This was done to allow enough time for the temperature-driven mechanical relaxation to occur and achieve a good baseline for the recording of stress response during cycling. The cell was cycled at a rate of C/5 in the voltage range of 1.35–2.85 V vs $Li_4Ti_5O_{12}$/$Li_7Ti_5O_{12}$ using a VMP3 multichannel potentiostat (BioLogic).

4.7. CV

CV measurements were conducted using the same setup described in the pressure-monitoring experiment. They were performed in the voltage range of OCV-2.85 V for the first cycle and 0–2.85 V vs $Li_4Ti_5O_{12}$/$Li_7Ti_5O_{12}$ for the subsequent cycles at a sweep rate of 0.05 mV s^{-1} using a VMP3 multichannel potentiostat. The positive electrode consisted of either glassy 1.5Li_2S-0.5P_2S_5-LiI or argyrodite Li_6PS_5Cl SE and Super C65 carbon black with the weight ratio of 7.5:2.5. The anode composite was similar to that used in the electrochemical measurements.

4.8. SEM

Cathode pellets/sheets were recovered from the cells in an Ar-filled glovebox. The samples were then mounted onto a sample holder using conductive carbon tape and probed using cross-sectional SEM at 10 kV.

4.9. DEMS

The cells consisted of a slurry-cast cathode, an SE pellet separator (glassy 1.5Li_2S-0.5P_2S_5-LiI or argyrodite Li_6PS_5Cl), and an In-foil anode. They were assembled in a method described in previous publications [37, 55]. Galvanostatic cycling was done at a rate of C/20 and 45 °C in the voltage range of 2.3–4.4 V vs In/InLi using a VMP3 multichannel potentiostat. A 10 h OCV period was included in the beginning to allow the cell to stabilize at the temperature and establish a proper background for the mass spectrometer. The flow of carrier gas (2.5 ml min^{-1}, 6.0 helium) was controlled by a mass flow controller (F-201CV, Bronkhorst). For gas analysis, a mass spectrometer (OmniStar GSD 320 O2, Pfeiffer Vacuum GmbH) was used. After each measurement, a calibration gas was introduced to convert the measured ion currents into mol/g values.

4.10. XPS

XPS analysis was carried out with a PHI5000 Versa Probe II system (Physical Electronics GmbH). Analogous to previous studies, the samples were attached to the sample holder using nonconducting adhesive tape [27, 60, 61]. During the measurement, a dual-beam charge neutralization was applied. Additionally, depth profiling was done to clean the surface in order to reduce the influence of degradation processes at the current collector/SE interface. For analysis, a monochromatic Al-Kα radiation (1486.6 eV) was used. The x-ray source was operated with a power of 50 W and voltage between 15 and 17 kV. The experimental data were evaluated using the software CasaXPS (version 2.3.22, Casa Software Ltd). The energy calibration was performed similarly to previous studies [27, 60, 63]. The x-ray photoelectron) spectra of all composite cathodes were calibrated in relation to the energetic signal position of the main component of the S 2p signal (PS_4^{3-}) at 161.7 eV in order to avoid detrimental surface effects and misleading energy calibration when using the C 1s signal. The suitability of the energy calibration was verified with other main components of the SE. For signal fitting, Shirley background, GL(30) line shapes, and common fitting restrictions were applied [67].

4.11. ToF-SIMS

ToF-SIMS analysis was performed with a TOF.SIMS 5–100 system (IONTOF GmbH). It is equipped with a 25 keV Bi cluster primary-ion gun for analysis and a dual-source column, enabling depth profiling by using either O_2^+ or Cs^+ (up to 2 keV). In addition, a FIB option can be used to mill craters

with monatomic gallium (30 keV). The samples were attached to the sample holder using nonconductive adhesive tape. The sample surface was flooded with low-energy electrons for charge compensation. All measurements were done in negative ion mode using Bi_3^+ species (25 keV) for analysis and a cycle time of 60 μs. Surface analysis was performed by operating the instrument in spectrometry mode (bunched mode). This mode enables high signal intensities and a high mass resolution [FWHM $m/\Delta m > 4500$ for $m/z = 31.97$ (S^-)], thereby minimizing effects of signal interferences in the mass spectra. The analysis area was set to 150 $\times$ 150 μm^2 and rasterized with 256 $\times$ 256 pixels. Every patch was analyzed with one frame and one shot per pixel and frame. For comparable measuring conditions, the analysis was stopped after a primary-ion dose of 1×10^{12} ions cm^{-2} (static conditions). The primary-ion current was ~0.5 pA. Ten mass spectra per sample were measured in different areas on the surface to alleviate area-dependent effects and ensure the reproducibility of results (increase statistics). The evaluation of ToF-SIMS data was done with the software SurfaceLab 7.0 (IONTOF GmbH). All secondary ion images were normalized in relation to the total ion signal to mitigate topographic effects. The signal intensities were extracted from the respective normalized secondary ion images.

Acknowledgments

This study was supported by BASF SE. F Strauss acknowledges financial support from the Fonds der Chemischen Industrie through a Liebig fellowship.

ORCID iD

Torsten Brezesinski https://orcid.org/0000-0002-4336-263X

References

[1] Blomgren G E 2017 *J. Electrochem. Soc.* **164** A5019–25
[2] Tarascon J-M and Armand M 2001 *Nature* **414** 359–67
[3] Larcher D and Tarascon J-M 2015 *Nat. Chem.* **7** 19–29
[4] Wang Q, Ping P, Zhao X, Chu G, Sun J and Chen C 2012 *J. Power Sources* **208** 210–24
[5] Etacheri V, Marom R, Elazari R, Salitra G and Aurbach D 2011 *Energy Environ. Sci.* **4** 3243–62
[6] Janek J and Zeier W G 2016 *Nat. Energy* **1** 16141
[7] Conforto G, Ruess R, Schröder D, Trevisanello E, Fantin R, Richter F H and Janek J 2021 *J. Electrochem. Soc.* **168** 070546
[8] Ruess R, Schweidler S, Hemmelmann H, Conforto G, Bielefeld A, Weber D A, Sann J, Elm M T and Janek J 2020 *J. Electrochem. Soc.* **167** 100532
[9] Ma Y, Teo J H, Kitsche D, Diemant T, Strauss F, Ma Y, Goonetilleke D, Janek J, Bianchini M and Brezesinski T 2021 *ACS Energy Lett.* **6** 3020–8
[10] de Biasi L, Kondrakov A O, Geßwein H, Brezesinski T, Hartmann P and Janek J 2017 *J. Phys. Chem.* C **121** 26163–71
[11] Jung S H, Kim U-H, Kim J-H, Jun S, Yoon C S, Jung Y S and Sun Y-K 2020 *Adv. Energy Mater.* **10** 1903360
[12] Li W, Erickson E M and Manthiram A 2020 *Nat. Energy* **5** 26–34
[13] Deng Z, Wang Z, Chu I-H, Luo J and Ong S P 2016 *J. Electrochem. Soc.* **163** A67–A74
[14] McGrogan F P, Swamy T, Bishop S R, Eggleton E, Porz L, Chen X, Chiang Y-M and Van Vliet K J 2017 *Adv. Energy Mater.* **7** 1602011
[15] Kato A, Yamamoto M, Sakuda A, Hayashi A and Tatsumisago M 2018 *ACS Appl. Energy Mater.* **1** 1002–7
[16] Han F, Yue J, Zhu X and Wang C 2018 *Adv. Energy Mater.* **8** 1703644
[17] Han Y, Jung S H, Kwak H, Jun S, Kwak H H, Lee J H, Hong S-T and Jung Y S 2021 *Adv. Energy Mater.* **11** 2100126
[18] Koerver R, Aygün I, Leichtweiß T, Dietrich C, Zhang W, Binder J O, Hartmann P, Zeier W G and Janek J 2017 *Chem. Mater.* **29** 5574–82
[19] Park K H, Bai Q, Kim D H, Oh D Y, Zhu Y, Mo Y and Jung Y S 2018 *Adv. Energy Mater.* **8** 1800035
[20] Richards W D, Miara L J, Wang Y, Kim J C and Ceder G 2016 *Chem. Mater.* **28** 266–73
[21] Wang S, Xu H, Li W, Dolocan A and Manthiram A 2018 *J. Am. Chem. Soc.* **140** 250–7
[22] Takada K, Ohta N, Zhang L, Fukuda K, Sakaguchi I, Ma R, Osada M and Sasaki T 2008 *Solid State Ion.* **179** 1333–7
[23] Ohta N, Takada K, Sakaguchi I, Zhang L, Ma R, Fukuda K, Osada M and Sasaki T 2007 *Electrochem. Commun.* **9** 1486–90
[24] Machida N, Kashiwagi J, Naito M and Shigematsu T 2012 *Solid State Ion.* **225** 354–8
[25] Kim A-Y, Strauss F, Bartsch T, Teo J H, Hatsukade T, Mazilkin A, Janek J, Hartmann P and Brezesinski T 2019 *Chem. Mater.* **31** 9664–72
[26] Strauss F, Teo J H, Maibach J, Kim A-Y, Mazilkin A, Janek J and Brezesinski T 2020 *ACS Appl. Mater. Interfaces* **12** 57146–54
[27] Walther F, Randau S, Schneider Y, Sann J, Rohnke M, Richter F H, Zeier W G and Janek J 2020 *Chem. Mater.* **32** 6123–36
[28] Wang S *et al* 2021 *Adv. Energy Mater.* **11** 2100654
[29] Strauss F, Teo J H, Janek J and Brezesinski T 2020 *Inorg. Chem. Front.* **7** 3953–60
[30] Koerver R, Zhang W, de Biasi L, Schweidler S, Kondrakov A O, Kolling S, Brezesinski T, Hartmann P, Zeier W G and Janek J 2018 *Energy Environ. Sci.* **11** 2142–58
[31] Shi T, Zhang Y-Q, Tu Q, Wang Y, Scott M C and Ceder G 2020 *J. Mater. Chem.* A **8** 17399–404
[32] Strauss F, de Biasi L, Kim A-Y, Hertle J, Schweidler S, Janek J, Hartmann P and Brezesinski T 2020 *ACS Mater. Lett.* **2** 84–8
[33] Reuter F, Baasner A, Pampel J, Piwko M, Dörfler S, Althues H and Kaskel S 2019 *J. Electrochem. Soc.* **166** A3265–A3271
[34] Chen S, Zhang J, Nie L, Hu X, Huang Y, Yu Y and Liu W 2021 *Adv. Mater.* **33** 2002325
[35] Minnmann P, Quillman L, Burkhardt S, Richter F H and Janek J 2021 *J. Electrochem. Soc.* **168** 040537
[36] Kim M-J, Park J-W, Kim B G, Lee Y-J, Ha Y-C, Lee S-M and Baeg K-J 2020 *Sci. Rep.* **10** 11923
[37] Teo J H, Strauss F, Tripković Đ, Schweidler S, Ma Y, Bianchini M, Janek J and Brezesinski T 2021 *Cell Rep. Phys. Sci.* **2** 100465
[38] Zhang W, Schröder D, Arlt T, Manke I, Koerver R, Pinedo R, Weber D A, Sann J, Zeier W G and Janek J 2017 *J. Mater. Chem.* A **5** 9929–36
[39] Zhang W *et al* 2017 *ACS Appl. Mater. Interfaces* **9** 17835–45
[40] Sakuda A, Hayashi A and Tatsumisago M 2010 *Chem. Mater.* **22** 949–56

[41] Ohzuku T, Ueda A and Yamamoto N 1995 *J. Electrochem. Soc.* **142** 1431–5
[42] Wagemaker M, Simon D R, Kelder E M, Schoonman J, Ringpfeil C, Haake U, Lützenkirchen-Hecht D, Frahm R and Mulder F M 2006 *Adv. Mater.* **18** 3169–73
[43] Haetge J, Hartmann P, Brezesinski K, Janek J and Brezesinski T 2011 *Chem. Mater.* **23** 4384–93
[44] Sun G, Sui T, Song B, Zheng H, Lu L and Korsunsky A M 2016 *Extreme Mech. Lett.* **9** 449–58
[45] Sakuda A, Hayashi A, Takigawa Y, Higashi K and Tatsumisago M 2013 *J. Ceram. Soc. Japan* **121** 946–9
[46] Wang S *et al* 2021 *Adv. Energy Mater.* **11** 2101370
[47] Ujiie S, Hayashi A and Tatsumisago M 2013 *J. Solid State Electrochem.* **17** 675–80
[48] Ujiie S, Hayashi A and Tatsumisago M 2012 *Solid State Ion.* **211** 42–5
[49] Auvergniot J, Cassel A, Ledeuil J-B, Viallet V, Seznec V and Dedryvère R 2017 *Chem. Mater.* **29** 3883–90
[50] Bernhard R, Meini S and Gasteiger H A 2014 *J. Electrochem. Soc.* **161** A497–A505
[51] Calpa M, Rosero-Navarro N C, Miura A, Jalem R, Tateyama Y and Tadanaga K 2021 *Appl. Mater. Today* **22** 100918
[52] Jung R, Metzger M, Maglia F, Stinner C and Gasteiger H A 2017 *J. Electrochem. Soc.* **164** A1361–A1377
[53] Jung R, Strobl P, Maglia F, Stinner C and Gasteiger H A 2018 *J. Electrochem. Soc.* **165** A2869–A2879
[54] Bartsch T, Strauss F, Hatsukade T, Schiele A, Kim A-Y, Hartmann P, Janek J and Brezesinski T 2018 *ACS Energy Lett.* **3** 2539–43
[55] Strauss F, Teo J H, Schiele A, Bartsch T, Hatsukade T, Hartmann P, Janek J and Brezesinski T 2020 *ACS Appl. Mater. Interfaces* **12** 20462–8
[56] Wandt J, Freiberg A T S, Ogrodnik A and Gasteiger H A 2018 *Mater. Today* **21** 825–33
[57] Jung R, Metzger M, Maglia F, Stinner C and Gasteiger H A 2017 *J. Phys. Chem. Lett.* **8** 4820–5
[58] Mahne N, Renfrew S E, McCloskey B D and Freunberger S A 2018 *Angew. Chem., Int. Ed.* **57** 5529–33
[59] Hatsukade T, Schiele A, Hartmann P, Brezesinski T and Janek J 2018 *ACS Appl. Mater. Interfaces* **10** 38892–9
[60] Walther F, Strauss F, Wu X, Mogwitz B, Hertle J, Sann J, Rohnke M, Brezesinski T and Janek J 2021 *Chem. Mater.* **33** 2110–25
[61] Auvergniot J, Cassel A, Foix D, Viallet V, Seznec V and Dedryvère R 2017 *Solid State Ion.* **300** 78–85
[62] Dietrich C, Koerver R, Gaultois M W, Kieslich G, Cibin G, Janek J and Zeier W G 2018 *Phys. Chem. Chem. Phys.* **20** 20088–95
[63] Walther F, Koerver R, Fuchs T, Ohno S, Sann J, Rohnke M, Zeier W G and Janek J 2019 *Chem. Mater.* **31** 3745–55
[64] Minami K, Hayashi A and Tatsumisago M 2010 *Solid State Ion.* **181** 1505–9
[65] Franke R, Chassé T, Streubel P and Meisel A 1991 *J. Electron Spectrosc. Relat. Phenom.* **56** 381–8
[66] Cronau M, Szabo M, König C, Wassermann T B and Roling B 2021 *ACS Energy Lett.* **6** 3072–7
[67] Vizintin A, Lozinšek M, Chellappan R K, Foix D, Krajnc A, Mali G, Drazic G, Genorio B, Dedryvère R and Dominko R 2015 *Chem. Mater.* **27** 7070–81